First-principles study of crystalline and amorphous $Ge_2Sb_2Te_5$ and the effects of stoichiometric defects

2009 J. Phys.: Condens. Matter 21 255501

(http://iopscience.iop.org/0953-8984/21/25/255501)

J. Phys.: Condens. Matter **21** (2009) 499803 (1pp) doi:10.1088/0953-8984/21/49/499803

Corrigendum

First principles study of crystalline and amorphous $Ge_2Sb_2Te_5$ and the effects of stoichiometric defects
S Caravati, M Bernasconi, T D Kühne, M Krack and M Parrinello 2009 *J. Phys.: Condens. Matter* **21** 255501

Figure 11 reporting the projections of the electronic density of states on s, p and d pseudowavefunctions was actually obtained from an orthogonalized set of pseudowavefunctions and did not follow the definition given in section 2 of the paper. The correct projections are reported in the revised figure below. The contribution from d wavefunctions is negligible on the scale of the figure and has been omitted.

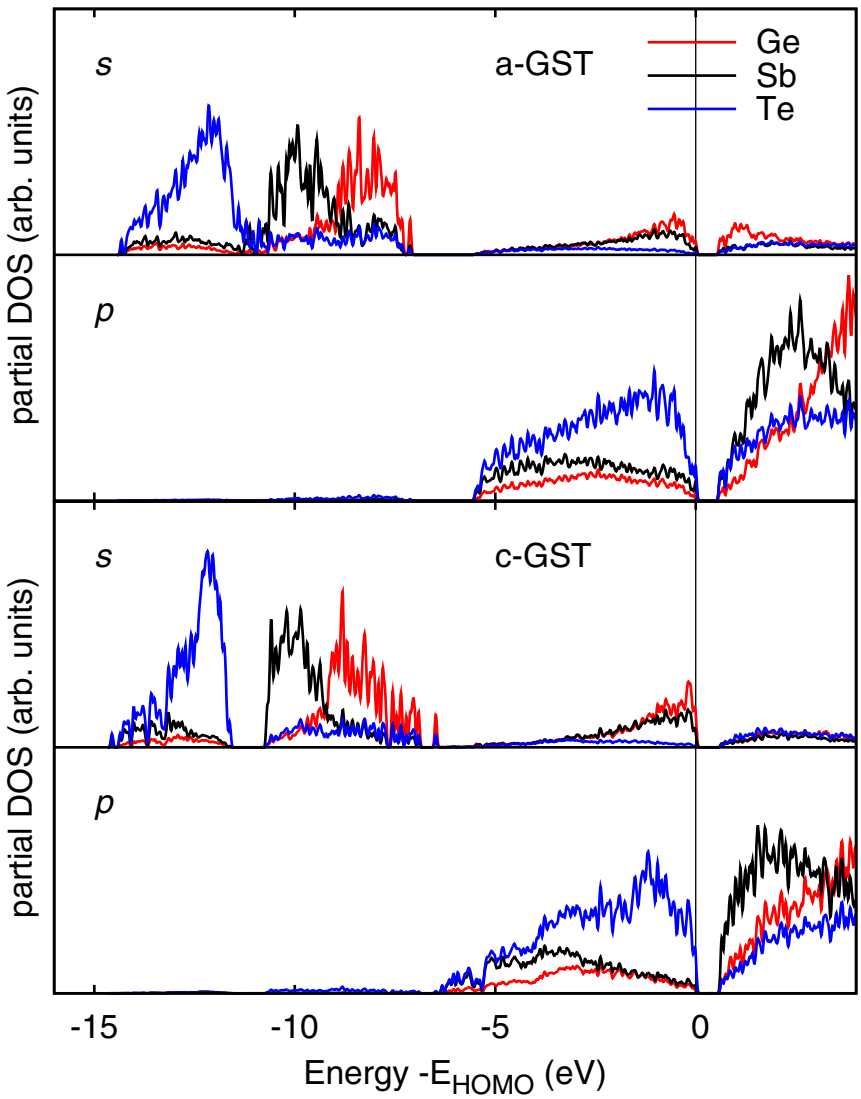

J. Phys.: Condens. Matter **21** (2009) 255501 (14pp) doi:10.1088/0953-8984/21/25/255501

First-principles study of crystalline and amorphous $Ge_2Sb_2Te_5$ and the effects of stoichiometric defects

S Caravati[1,2], M Bernasconi[1,3], T D Kühne[2], M Krack[4] and M Parrinello[2]

[1] Dipartimento di Scienza dei Materiali, Università di Milano-Bicocca, Via R Cozzi 53, I-20125, Milano, Italy
[2] Department of Chemistry and Applied Biosciences, ETH Zurich, USI Campus, Via Giuseppe Buffi 13, CH-6900 Lugano, Switzerland
[3] CNISM, Università di Milano-Bicocca, Via R Cozzi 53, I-20125, Milano, Italy
[4] Paul Scherrer Institut, CH-5232 Villigen, Switzerland

E-mail: marco.bernasconi@mater.unimib.it

Received 23 February 2009, in final form 7 May 2009
Published 1 June 2009
Online at stacks.iop.org/JPhysCM/21/255501

Abstract

Based on *ab initio* molecular dynamics simulations, we investigated the structural, electronic and vibrational properties of cubic and amorphous $Ge_2Sb_2Te_5$ (GST) phase change material, focusing in particular on the effects of defects in stoichiometry on the electronic properties. It turned out Ge/Sb deficiencies (excess) in the cubic phase induce a shift of the Fermi level inside the valence (conduction) bands. In contrast, the amorphous network is flexible enough to accommodate defects in stoichiometry, keeping the Fermi level pinned at the center of the bandgap (at zero temperature). Changes in the structural and electronic properties induced by the use of hybrid functionals (HSE03, PBE0) instead of gradient corrected functionals (PBE) are addressed as well. Analysis of vibrational spectra and Debye–Waller factors of cubic and amorphous GST is also presented.

(Some figures in this article are in colour only in the electronic version)

1. Introduction

Information storage based on phase change materials is widely used in optical technologies and it is presently considered as a promising alternative to flash memories for the non-volatile memory technology of the next decade [1–3]. A phase change non-volatile memory (PCM) is essentially a resistor made of a thin film of chalcogenide material with a low field resistance which changes by several orders of magnitude across the phase change, the system being highly conductive in the crystalline form and insulating in the amorphous phase. In the memory operation, cell readout is performed at low bias. Programing the memory requires instead a relatively large current to heat up the material and induce the phase change, either the melting of the crystal and subsequent amorphization or the recrystallization of the amorphous phase. The amorphous phase has a large resistance at low bias, but above a threshold voltage (typically a few volts in PCM) it switches to a highly conductive state which allows heating via the Joule effect and recrystallization [1, 2].

In the last few years, substantial progress has been made in the understanding of the basic properties of $Ge_2Sb_2Te_5$ (GST), which is presently the material of choice for PCM, and other compounds in the same class [1, 3]. In particular, *ab initio* calculations have provided crucial insight into the properties of amorphous GST (a-GST) [4–10]. However, several details of the electronic structure of the amorphous phase which are supposed to control the transport properties and the switching mechanism are still a matter of debate. For instance, subthreshold conductivity in a-GST is thermally activated and follows an Arrhenius law with an activation energy of 0.4 eV [1, 11]. This behavior was interpreted as due to a low density of thermally generated carriers with high mobility outside the mobility gap [1, 12]. However, the different sign of the charge carriers in the measured Seebeck coefficient (p-type) and Hall mobility (n-type) suggested that

conductivity might be due to small polaron hopping with a high density of carriers in Urbach tails with low mobility inside the mobility gap [11]. In analogy with other chalcogenides, such as As_2Se_3 [13], it has been proposed that the Fermi level could be pinned near midgap by valence alternation pair (VAP) defects [2]. A Poole–Frenkel mechanism for subthreshold transport in the presence of a high concentration of trap states was also proposed [14]. Defect states in the gap are supposed to play a role in the switching, but the atomistic nature of these defects is still unknown [14]. On the other hand, in the metastable cubic (rocksalt) phase of GST involved in the transformation, defects in stoichiometry are supposed to generate a high density of holes in the valence band which turns the crystal into a p-type degenerate semiconductor [15]. The models developed so far for electronic transport in GST and related amorphous materials are, however, phenomenological in nature and are lacking in an experimentally grounded atomistic description. In this respect, *ab initio* modeling can provide useful information for the development of effective phenomenological models for electronic transport.

In this paper, we extend our previous work on amorphous GST [4] by studying crystalline and amorphous GST with stoichiometric defects, aiming at understanding the dependence of the position of the Fermi level on a small deviation in stoichiometry. Models of amorphous GST with stoichiometric defects were generated by quenching from the melt within the density-functional-based molecular dynamics scheme used in our previous work [4]. To describe possible localized electronic states in the bandgap, we employed a hybrid exchange–correlation functional (HSE03 [16]) which also allowed assessing the dependence of the structural properties on the choice of exchange and correlation functional. Additional information on the properties of stoichiometric a-GST and c-GST are provided by reporting the analysis of the vibrational spectrum and Debye–Waller factors.

2. Computational details

Ab initio molecular dynamics simulations were performed using the scheme of Kühne *et al* [17]. In the spirit of the Car–Parrinello (CP) approach the wavefunctions are not self-consistently optimized during the dynamics. However, in contrast to CP, large integration time steps can be used in the simulation. This scheme leads to a slightly dissipative dynamics of the type $-\gamma_D\dot{\mathbf{R}}_I$, where $\mathbf{R}_I$ are the ionic coordinates. In [17] it is shown how to compensate for this dissipation and obtain a correct canonical sampling. This scheme is implemented in the CP2K suite of programs [18, 19]. We used the Perdew–Burke–Ernzerhof (PBE) exchange correlation functional [20] and Goedecker-type pseudopotentials [21]. Four-, five-and six-valence electrons were considered for Ge, Sb and Te, respectively. The Kohn–Sham orbitals were expanded in a triple-zeta-valence plus polarization (TZVP) Gaussian-type basis set and the charge density was expanded in a plane wave basis set with a cutoff of 100 Ryd to efficiently solve the Poisson equation within the Quickstep scheme [18, 19]. Brillouin zone integration was restricted to supercell Γ points. A time step of 2.5 and 2 fs were used for the sample preparation and data collection simulations, respectively.

The initial configuration for the generation of the amorphous models was the metastable cubic GST (c-GST) where Te occupies one sublattice of the rocksalt crystal while Ge, Sb and vacancies are randomly placed in the other sublattice [22–24]. We used an orthorhombic supercell of size $21.97 \times 21.97 \times 18.63$ Å^3 (270 atoms) at the density of 0.030 atoms Å^{-3} close to the experimental value for a-GST [25]. Then we added 6 Ge atoms in vacancy positions (10% Ge excess) or we removed 6 Sb atoms (10% Sb deficiency). The two models were heated and equilibrated for 27 ps at 980 K and then quenched at 500 K for 50 ps and at 300 K for an additional 10 ps. The parameter $\gamma_D = 4 \times 10^{-4}$ fs^{-1} was determined as in [17]. We have also generated a model of stoichiometric GST with the same quenching protocol as given above (slow-quenched model), a factor of three longer than the quenching time (18 ps) used in our previous simulation (fast-quenched model) [4]. Besides the two compositions discussed above, we generated other models of off-stoichiometric cubic GST (270 atoms) by adding/removing Ge/Sb in different amounts and fixing the lattice parameter at the experimental value for stoichiometric c-GST [22].

To describe possible localized states in the bandgap, we computed the electronic properties of the models relaxed at the DFT-PBE level of theory by making use of hybrid functionals which better reproduce the bandgap with respect to the PBE functional. Among the different functionals we tried (PBE0 [26], HSE03 [16], HSE06 [27], TPSS0 [28], TPSSh [28]), we chose the HSE03 functional since it was the best in reproducing the bandgap of our model of cubic GST. The theoretical bandgap of cubic GST turned out to be 0.6 eV, to be compared with the experimental value of 0.5 eV [15]. In contrast with the PBE functional the bandgap of our models of cubic GST is as low as 0.37 eV.

Electronic density of states (DOS) of the models was obtained from Kohn–Sham (KS) energies at the supercell Γ-point broadened with a Gaussian function with variance of 27 meV. To quantify the localization properties of individual KS states, we computed the inverse participation ratio (IPR) which is defined for the ith KS state by $\sum_j c_{ij}^4/(\sum_j c_{ij}^2)^2$, where j runs over the Gaussian-type orbitals (GTOs) of the basis set and c_{ij} are the expansion coefficients of the ith KS state in GTOs.

The amorphous model of stoichiometric GST was also further optimized with the HSE03 functional to assess the dependence of the structural properties on the exchange–correlation functional. Theoretical equilibrium volumes of c-GST and a-GST were also computed at the PBE level and within the simple local density approximation (LDA).

3. Results

3.1. Crystalline phases

The electronic density of states of stoichiometric and off-stoichiometric models of crystalline GST calculated with the

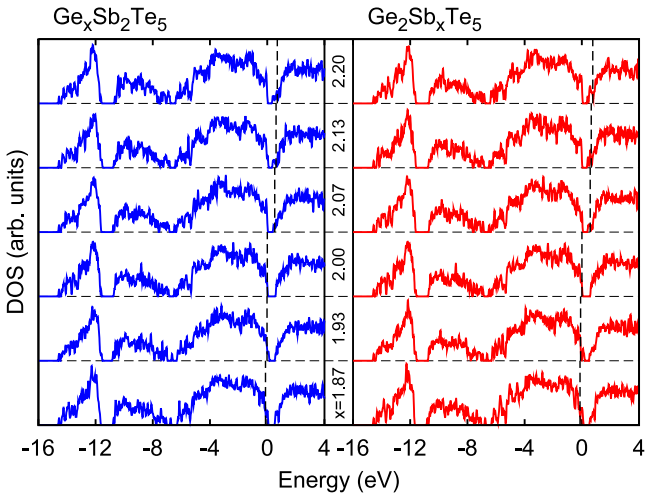

Figure 1. Electronic density of states of the cubic crystal with different amounts of Ge (left panels, blue curves) and Sb (right panels, red curves) excess/deficiency. From the bottom to the top, the amount of Ge/Sb is increasing from a deficiency of 4 atoms (bottommost panels) to an excess of 6 atoms in the Sb/Ge sublattice of a 270-atom supercell (topmost panels). The Te sublattice is fully occupied by Te. Vertical dashed lines denote the Fermi level for off-stoichiometric GST or the highest occupied molecular orbital in stoichiometric GST since the Fermi level lies at the center of the bandgap for the latter system. The zero of energy is the top of the valence band in stoichiometric GST. The DOS of off-stoichiometric models are aligned near the bottom of the deepest structure of the valence band to the corresponding value in the stoichiometric compound.

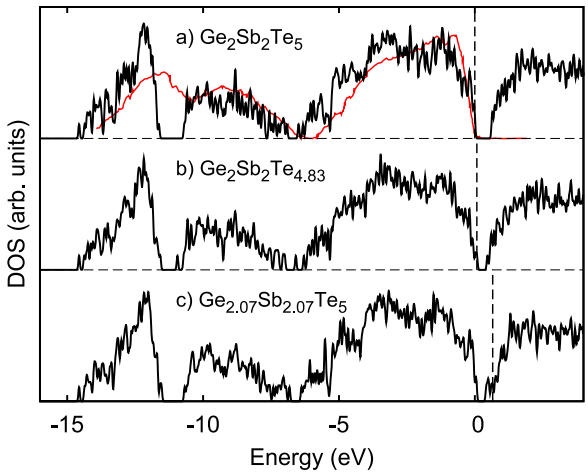

Figure 2. Electronic density of states (DOS) of crystals (a) with stoichiometric composition (b) with Te deficiency in the form of vacancies in Te sublattice ($Ge_2Sb_2Te_{4.83}$), (c) nearly the same composition of panel (b) generated by adding Ge/Sb in the corresponding sublattice with the Te sublattice fully occupied ($Ge_{2.07}Sb_{2.07}Te_5$). The zero of energy is the top of the valence band in stoichiometric GST. The DOS of off-stoichiometric GST are plotted by aligning the bottom of the deepest structure of the valence band to the corresponding value in the stoichiometric compound. Vertical dashed lines denote the Fermi level for off-stoichiometric GST or the highest occupied molecular orbital in stoichiometric GST since the Fermi level lies at the center of the bandgap for the latter system. The thin (red) line in panel (a) is the experimental DOS measured by x-ray photoelectron spectroscopy [33]. The HSE03 DOS extends to lower energies by 1 eV with respect to the PBE DOS [6] which results in a worse agreement with experiments in the position of the maximum below −10 eV.

HSE03 functional are reported in figure 1. All the systems are generated by adding or removing Sb/Ge atoms from the Ge/Sb sublattice. The Te sublattice is fully occupied by Te.

At stoichiometric composition, cubic GST is a semiconductor as the 20% constitutional vacancies on the Ge/Sb sublattice are electrically inactive and they have not to be considered as 'defects' [10]. However, by adding (removing) additional vacancies via an increase of Sb or Ge deficiency (excess), the Fermi level shifts progressively into the valence (conduction) bands (figure 1). Similar results have been reported for the related compound GeTe by Edwards *et al* [29] who, based on *ab initio* calculations, have shown that, while stoichiometric GeTe is insulating, Ge vacancies induce a shift of the Fermi level into the valence band consistent with the p-type metallic character measured experimentally [29]. Note that defects in stoichiometry due to Te deficiency in the form of vacancies in the Te sublattice do not induce a shift of the Fermi level. In figure 2 we report the DOS of the compound $Ge_2Sb_2Te_{4.83}$ generated by removing Te atoms from the corresponding lattice or by adding Ge and Sb atoms in the vacancies of the Ge/Sb sublattice ($Ge_{2.07}Sb_{2.07}Te_5$ nearly equivalent to $Ge_2Sb_2Te_{4.83}$). Although the composition is nearly the same, the position of the Fermi level depends on how the defects in stoichiometry are introduced. The highest occupied molecular orbital (HOMO) does shift in the conduction band for Ge/Sb excess but it is pinned at the top of the valence band when Te vacancies are introduced. Actually, introducing vacancies in the Te sublattice is sizably more costly than adding Sb/Ge into vacancy sites of the corresponding sublattice as shown in [30] for $GeSb_2Te_4$ and in [29] for GeTe. The same is true for GST as emerges from the calculation of the formation energies of neutral defects. The formation energies for vacancies (V_{Ge}, V_{Sb}, V_{Te}) and additional Ge or Sb filling vacancies (interstitials Ge_i and Sb_i) are strongly dependent on the actual environment (first and second coordination shells) of the defect which can vary because of the disorder in the Sb/Ge sublattice including vacancies. For each type of defect, we chose randomly nine different sites. The formation energies are computed with respect to c-GST and the standard crystalline states of Ge, Sb and Te optimized at the experimental lattice parameters with supercells containing up to 300 atoms and BZ integration restricted to the Γ-point. The resulting average formation energies with averaged square deviation are $E(V_{Ge}) = 0.63 \pm 0.39$ eV, $E(V_{Sb}) = 0.38 \pm 0.34$ eV, $E(V_{Te}) = 1.01 \pm 0.19$ eV, $E(Ge_i) = 0.31 \pm 0.20$ eV and $E(Sb_i) = 0.77 \pm 0.22$ eV. One concludes that a Te-deficient system is expected to have partial occupation of vacancy sites in the Sb/Ge sublattice with the Te sublattice completely filled. Moreover, since Sb vacancies are energetically favored with respect to Ge vacancies (as also shown for $GeSb_2Te_4$ in [30]) the degenerate p-type character of GST measured experimentally [15] is probably due to Sb deficiency. A more extensive analysis of the energetics of different defects in crystalline GST is postponed to a future work, as here we focus on the amorphous phase. To make a further comparison with

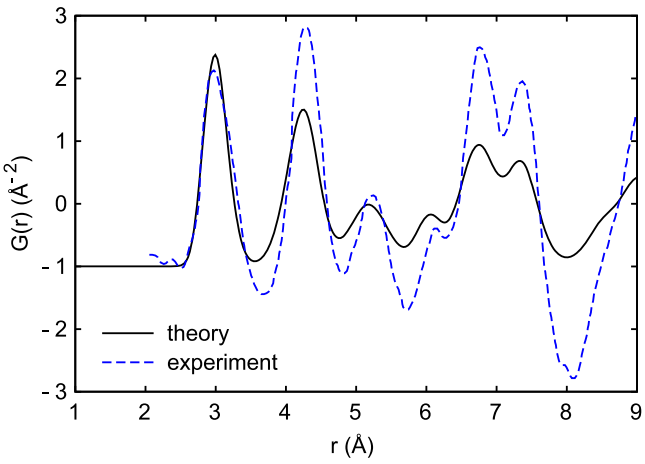

Figure 3. Neutron-weighted total pair correlation function, as defined by equation (10) in [31], calculated here (continuous line) for c-GST and measured experimentally (dashed line) by neutron diffraction in [32].

Table 1. Average coordination number for different pairs of atoms computed from the partial pair correlation functions (cf figures 4 and 6) for a-GST models at stoichiometric composition, with Sb deficiency and Ge excess. All the data correspond to the cutoff distances in figures 4 and 6. Experimental data in parentheses are inferred from EXAFS measurements in [37].

	With Ge	With Sb	With Te	Total
		$Ge_2Sb_2Te_5$		
Ge	0.29 (0.6 ± 0.2)	0.36	3.31 (3.3 ± 0.5)	3.96
Sb	0.36	0.43	3.36 (2.8 ± 0.3)	4.15
Te	1.33 (1.2 ± 0.3)	1.34 (1.2 ± 0.3)	0.30	2.97
		$Ge_2Sb_{1.80}Te_5$		
Ge	0.29	0.21	3.41	3.91
Sb	0.24	0.19	3.74	4.17
Te	1.36	1.35	0.28	2.99
		$Ge_{2.20}Sb_2Te_5$		
Ge	0.58	0.29	3.29	4.16
Sb	0.32	0.40	3.59	4.31
Te	1.45	1.43	0.24	3.12

experimental data we report in figure 3 the neutron-weighted total pair correlation function $G(r)$, as defined by equation (10) in [31], calculated here for stoichiometric c-GST and measured experimentally by neutron diffraction in [32]. Further details on the structural and vibrational properties of c-GST are given in section 3.2 in comparison with the results on the amorphous phase.

3.2. Amorphous phases

Structural properties. In a previous work we have generated a 270-atom model of amorphous GST by quenching from the melt within first-principles molecular dynamics. In our a-GST model [4], most of the Ge and Sb atoms are four-coordinated while Te is mostly three-coordinated in defective octahedral-like sites which recall the local environment of cubic crystalline GST. However, as many as one-third of Ge atoms are in a tetrahedral geometry, as proposed by extended x-ray absorption fine structure and x-ray absorption near-edge spectroscopy (EXAFS/XANES) measurements [34]. This configuration is absent in the crystalline phase and favored in a-GST by the presence of homopolar (Ge–Ge and Ge–Sb) bonds [4]. Similar results on the structural properties have been obtained from *ab initio* simulations by other groups [5–7]. The coexistence of defective octahedral sites (for Te and Ge) and tetrahedral sites (Ge only) have also been found for the related GeTe binary compound [5].

The structure of the off-stoichiometric a-GST models generated here is obviously similar to that of stoichiometric a-GST. Pair correlation functions, angle distribution functions, distribution of coordination numbers and distribution of the q order parameter for tetrahedricity introduced in [4] are given in figures 4–8 for stoichiometric and off-stoichiometric models of a-GST. Neutron-weighted total scattering functions $S(Q)$, as defined by equation (20) in [31], calculated here for a-GST and measured experimentally by neutron diffraction in [35], are compared in figure 5. The average coordination numbers for the different species computed from the partial pair correlation functions are given in table 1. The coordination numbers are obtained by integrating the pair correlation functions up to a cutoff distance of 3.2 Å for all species which corresponds to the outer edge of the Ge–Te pair correlation function, but for the Sb–Te pair whose correlation function displays a very broad first peak. For Sb–Te we have enlarged the cutoff distance up to the outer edge of the partial correlation function in the crystalline phase (cf figure 4). The change in coordination numbers with respect to our previous work [4] is partially due to the longer quenching time used here (with a reduction in the Ge–Ge pairs for the slow-quenched model, cf figure 4), but mostly to the choice made here of the same equal cutoff function for Ge–Te, Ge–Ge and Te–Te which seem more appropriate to describe also the nonstoichiometric compounds. Statistics of GeX_4 coordination environments for stoichiometric a-GST are given in figure 9. The results are similar to those reported by Akola and Jones [6] but somehow different from those of the RMC models of [35] which shows a larger contribution from other configurations. The disagreement might be partially due to the limited statistics accessible by the still small simulation cells.

We further optimized the a-GST model (fast-quenched) at the stoichiometric composition, obtained from MD simulations at the PBE level, by using the HSE03 and PBE0 hybrid functionals. The position of the first maximum of the partial pair correlation functions at the PBE and HSE03 level are compared in table 2 (cf figure 4). Values for a PBE0 [26] optimized model are the same (within the figures of the table) as the HSE03 values reported. Enlarging the basis set from TZVP to QZV2P does not introduce appreciable changes in the pair correlation functions. The hybrid functional generates bond lengths 2% shorter than the PBE results but still ∼5% too long when compared to the EXAFS data [34, 35, 37, 38] for Ge–Te (2.61–2.64 Å) and Sb–Te bond lengths (2.83–2.85 Å). On the other hand, the maximum of the total pair correlation function extracted from x-ray diffraction on as-deposited

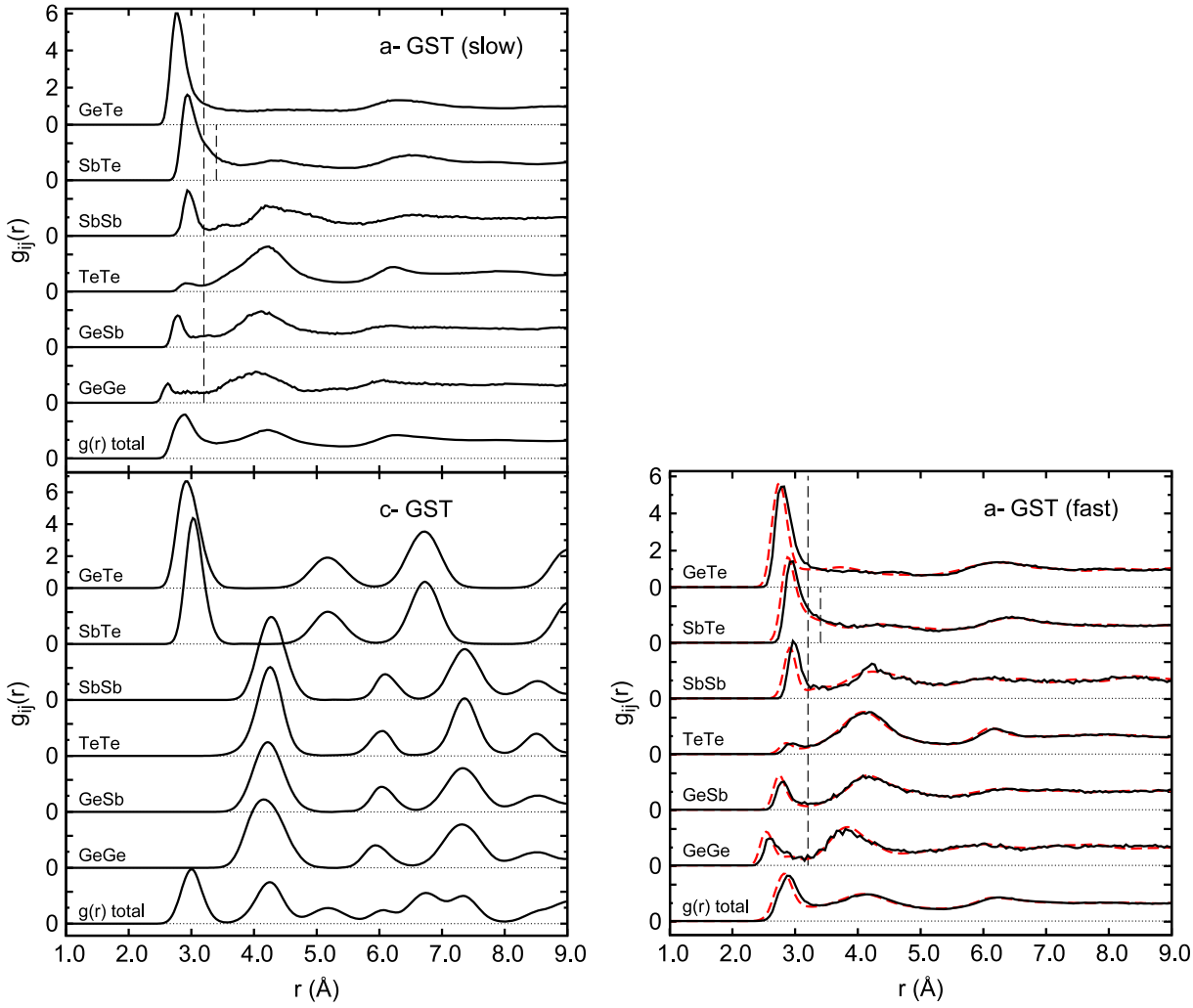

Figure 4. Left panel: total and partial pair correlation functions of amorphous (slow-quenched) and crystalline $Ge_2Sb_2Te_5$. Right panel: total and partial pair correlation functions of a-GST (fast-quenched) from [4]. Data are reported for the model optimized at the PBE (bold line) and HSE03 (dashed line) level of theory (see text). The vertical lines are the bonding cutoff used to define the coordination numbers (3.2 Å for all pairs but Sb–Te for which the outer edge of the partial pair correlation function of c-GST (300 K) was chosen). The pair correlation functions for c-GST and for a-GST with the HSE03 functional are obtained from the optimized geometry at zero temperature and harmonic PBE phonons weighted by the quantum Bose factors as outlined in [36].

a-GST is 2.74 Å [39], to be compared with our value of 2.83 Å.[5] All the discussions in [4] on the coexistence of tetrahedral and octahedral sites of Ge and on the analysis of ring distribution and angle distribution functions still hold. It agrees with the *ab initio* results by Akola and Jones [5, 6] and will not be repeated here.

We also computed the equation of state (at zero temperature) of c-GST and a-GST with a PBE functional by optimizing the internal structure at different volumes and fitting the energy–volume points with a Murnaghan function. The resulting equilibrium density of the amorphous and crystalline phases are $\rho_a = 0.0287$ atoms Å^{-3} and $\rho_c = 0.0311$ atoms Å^{-3}, respectively, to be compared with the corresponding experimental values of $\rho_a^{exp} = 0.031$ atoms Å^{-3} and $\rho_c^{exp} = 0.033$ atoms Å^{-3} [40]. The model of a-GST is 8% less dense than c-GST, in good agreement with

[5] We have also performed a 300 K equilibration of the stoichiometric model of GST by using a Te pseudopotential with semicore $4d^{10}$ electrons in the valence. The resulting pair correlation functions are indistinguishable from those reported in figure 4.

Table 2. Position (Å) of the first maximum of the partial pair correlation functions (cf figure 4) of a-GST at stoichiometric composition, optimized at the PBE level (slow-quenched model, see text). Values in parentheses correspond to the model optimized with the HSE03 hybrid functional starting from the model obtained from the PBE molecular dynamics simulations. Experimental values for Ge–Te and Sb–Te bond length from EXAFS [34, 35, 37, 38] are, respectively, in the range 2.61–2.64 Å and 2.83–2.85 Å. The maximum of the total pair correlation function extracted from x-ray diffraction on as-deposited a-GST is 2.74 Å [39] to be compared with our value of 2.89 Å (2.82 Å with the HSE03 functional).

	With Ge	With Sb	With Te
Ge	2.62 (2.54)	2.78 (2.75)	2.77 (2.75)
Sb		2.95 (2.92)	2.94 (2.88)
Te			2.92 (2.86)

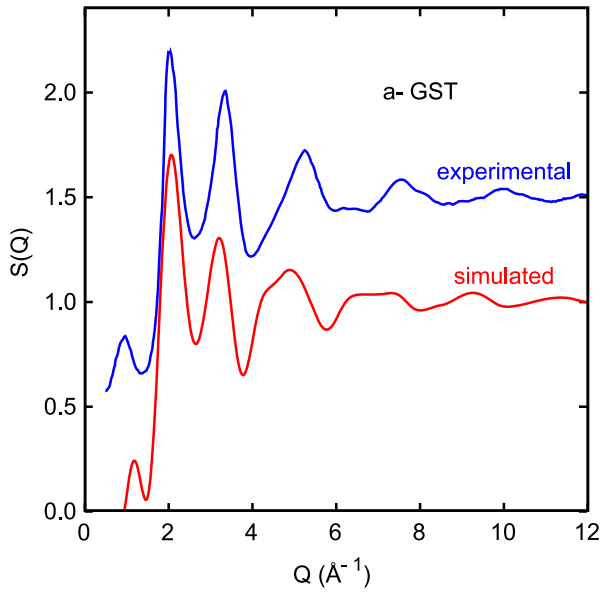

Figure 5. Neutron-weighted total scattering function $S(Q)$, as defined by equation (20) in [31], calculated here for a-GST and measured experimentally by neutron diffraction in [35].

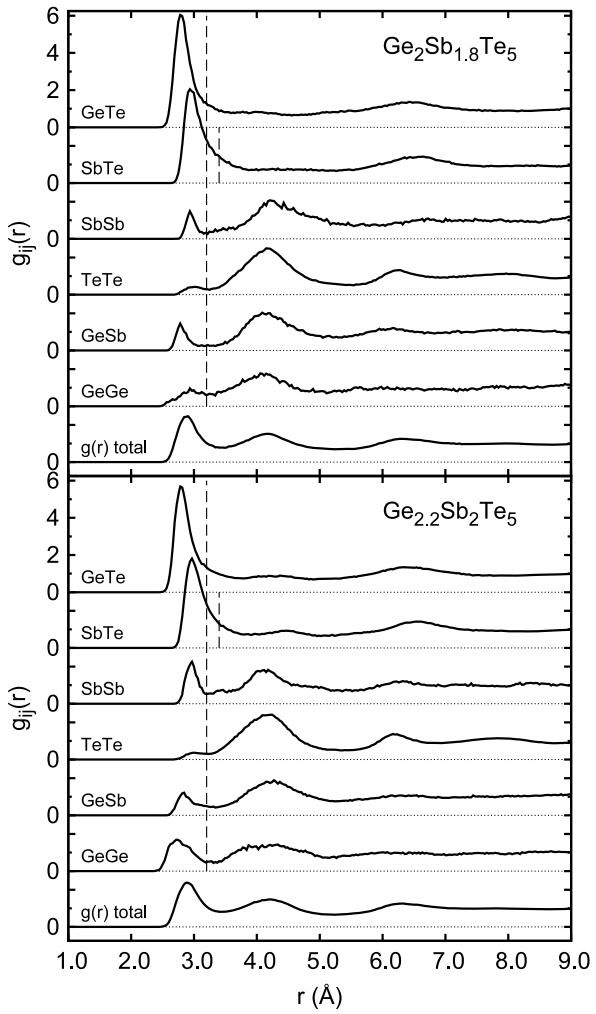

Figure 6. Total and partial pair correlation functions of a-GST with Sb deficiency (upper panel) and Ge excess (lower panel). The vertical lines are the bonding cutoff used to define the coordination numbers (3.2 Å for all pairs but Sb–Te for which the outer edge of the partial pair correlation function of c-GST (300 K) was chosen).

the corresponding experimental value of 6.3% [40]. The theoretical bulk moduli of c-GST and a-GST are 27 and 11 GPa. The experimental bulk modulus of c-GST measured in [41] is, however, 41 ± 2 GPa, a value substantially larger than our result. To assess the dependence of the equilibrium density and compressibility on the choice of the exchange and correlation functional, we repeated the calculation of the equation of states of c-GST and a-GST within the simple LDA. The resulting equilibrium densities are $\rho_a = 0.0329$ atoms Å^{-3} and $\rho_c = 0.0341$ atoms Å^{-3} which are closer to the experimental values (see above), although the change in density across the phase change is now only 3.5%. At the theoretical equilibrium density of a-GST, the position of the maxima of the pair correlation functions are at shorter distances with respect to the PBE results, although still sizably longer than the EXAFS data (cf table 2), namely 2.50 Å(Ge–Ge), 2.70 Å(Ge–Sb), 2.72 Å(Ge–Te), 2.90 Å(Sb–Sb) and 2.92 Å(Sb–Te).

The bulk modulus of c-GST is 40 GPa, close to the experimental value of 41 GPa in [41]. The bulk modulus of a-GST is 22 GPa, still much lower than that of c-GST. With both the PBE and LDA functionals, the amorphous phase is thus much more compressible than the crystal. This feature is the driving force of the pressure-induced amorphization of c-GST demonstrated experimentally in [41] and analyzed theoretically in our recent work [42].

Defects in stoichiometry do not induce sizable changes in the amorphous network, but for an overall increase in the coordination numbers for Ge excess. In contrast, Sb deficiencies induce only a marginal decrease in the coordination numbers.

Electronic properties. Turning now to the electronic properties, as opposed to what occurs in the crystal, Sb deficiency and Ge excess do not induce a shift of the Fermi level in the amorphous phase. The HOMO state is pinned at the top of the valence band in both off-stoichiometric models of a-GST shown in figure 10. The amorphous network is flexible enough to accommodate defects in stoichiometry still remaining insulating. Projection of the DOS of stoichiometric a-GST on s, p and d atomic pseudowavefunctions are given in figure 11 for each species for completeness. The electronic DOS of stoichiometric a-GST are similar to those at the PBE level reported previously [5, 6]. Due to the use of a different exchange and correlation functional, the DOS in figure 11 displays a larger bandgap closer to the experimental optical gap, but also a shift to lower energies of the lowest s-type peak in the valence which worsen somehow the comparison with the experimental XPS data (cf figure 11 and [5, 6, 33]).

In figure 12 we report a zoom of the DOS around the Fermi level and the corresponding IPR values (see section 2) of stoichiometric c-GST and of the models of a-GST generated here (slow-quenched) and in our previous work (fast-quenched) [4]. The states in the bandgap of a-GST from 0 to 0.7 eV are clearly more localized than states deeper in

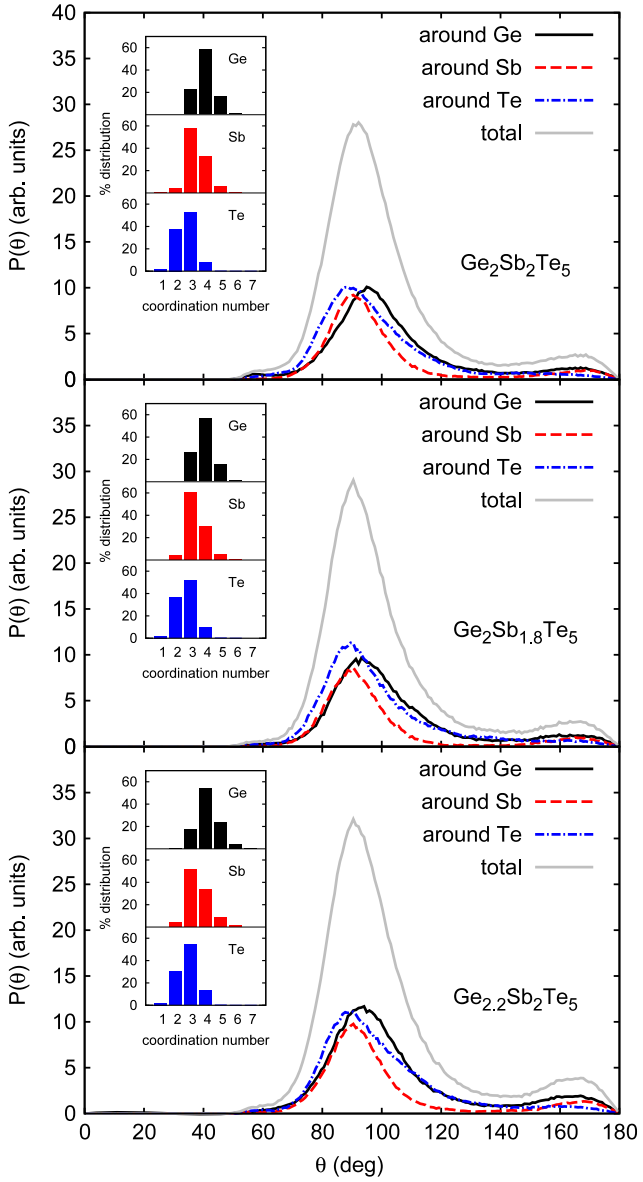

Figure 7. Angle distribution function of stoichiometric a-GST (upper panel), a-GST with Sb deficiency (central panel) and Ge excess (lower panel) at 300 K, total and resolved for different central atoms. Inset: distribution of coordination numbers of different species obtained by integration of the partial pair correlation functions (cf figures 4 and 6 and table 1).

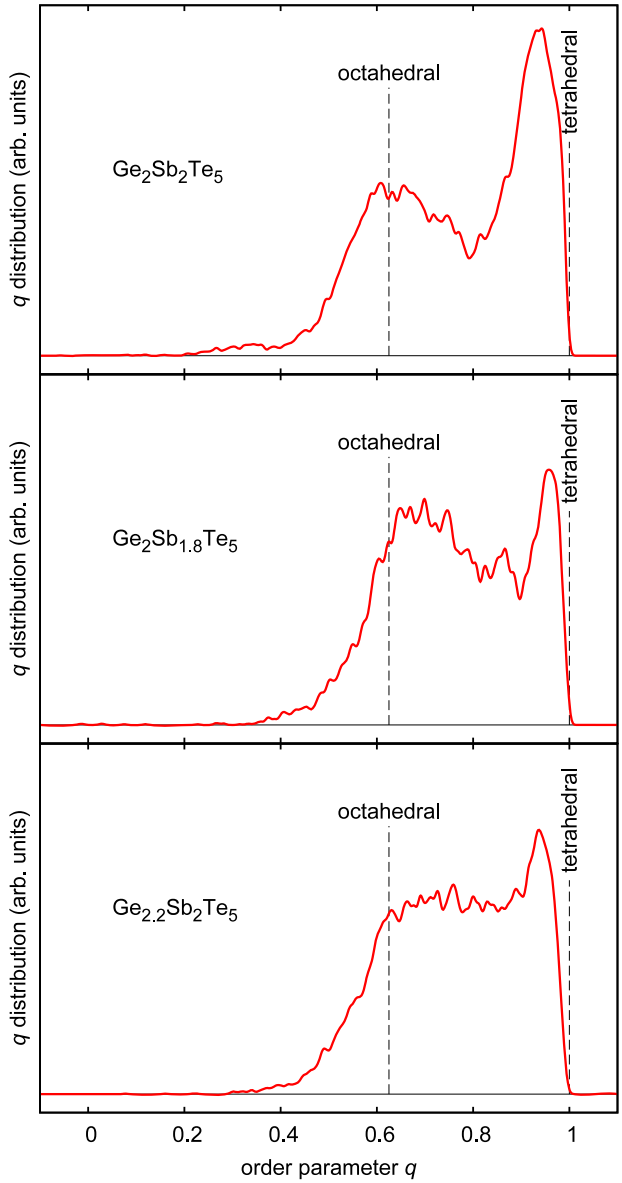

Figure 8. Distribution of the local order parameter q for four-coordinated Ge in stoichiometric a-GST (upper panel), a-GST with Sb deficiency (central panel) and Ge excess (lower panel) at normal conditions. The local order parameter q [4] is an indicator of the tetrahedral geometry defined by $q = \frac{1}{3} - \frac{3}{8}\sum_{i>k}(\frac{1}{3} + \cos\theta_{ijk})^2$, where the sum runs over the couples of atoms bonded to a central atom j. $q = 1$ for the ideal tetrahedral geometry, $q = 0$ for the six-coordinated octahedral site and $q = 5/8$ for a four-coordinated defective octahedral site. By integrating q from 0.8 to 1.0 we obtain a fraction of tetrahedral Ge atoms of 27% for the stoichiometric phase (slightly lower than the value of 33% of our previous fast-quenched model [4]), 25% for $Ge_2Sb_{1.8}Te_5$ and 23% for $Ge_{2.2}Sb_2Te_5$.

the valence and conduction bands. By defining the bandgap as the difference in energy between the outermost delocalized states at the two edges, the theoretical bandgap of a-GST turns out to be marginally larger than the bandgap of crystalline GST, in qualitative agreement with the measured optical Tauc gaps [15]. The midgap states present in the fast-quenched a-GST disappear in the slow-quenched model. Nevertheless, these latter states might also be present in (slow-quenched) real samples although with a concentration much lower than that found in our fast-quenched 270-atom model. In this respect, these states might be informative on the nature of possible (few) midgap states present in the real material. A snapshot of individual localized states in the bandgap of fast-quenched a-GST is given in figure 13. They correspond to orbitals mostly localized on chains of Sb and Te only. Note that the most localized state at the conduction band edge of crystalline GST is also localized on a straight chain of Sb and Te atoms which appeared in the process of generating the disordered cubic GST by a random number generator. Similarly, in the slow-quenched a-GST model, the most localized states near the edge of the conduction band are confined in Sb/Te chains

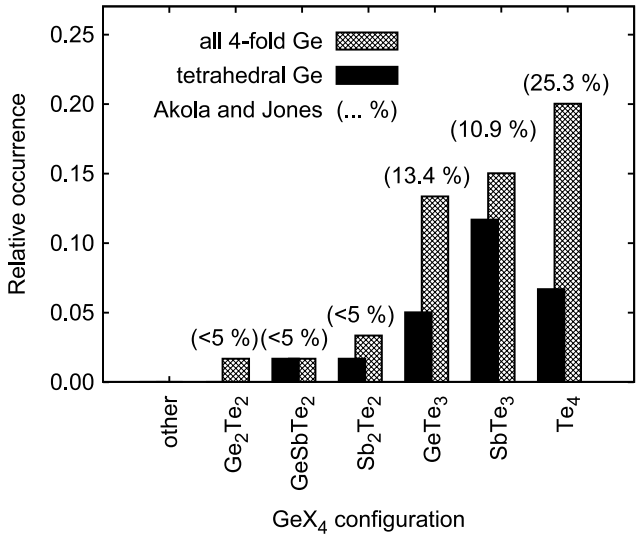

Figure 9. Statistics of GeX_4 coordination environments for stoichiometric a-GST. Relative occurrence refer to the whole number of Ge atoms (including three- and five-coordinated Ge). The values reported by Akola and Jones [6] are given in parentheses. In their model 53% of Ge are fourfold-coordinated (cf inset of figure 7).

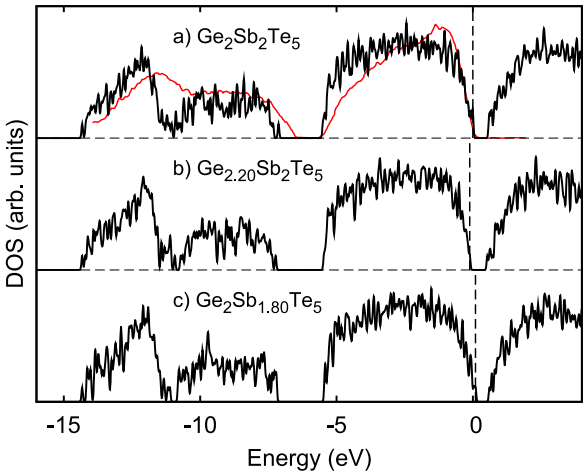

Figure 10. Electronic density of states of a-GST models (a) at stoichiometric composition, (b) with Ge excess ($Ge_{2.20}Sb_2Te_5$) and (c) with Sb deficiency ($Ge_2Sb_{1.80}Te_5$). The zero of energy is the top of the valence band in stoichiometric GST. The DOS of off-stoichiometric GST are plotted by aligning the bottom of the deepest structure of the valence band to the corresponding value in the stoichiometric compound. Vertical dashed lines denote the HOMO level which corresponds to the top of the valence band for all models. The thin (red) line in panel (a) is the experimental DOS measured by x-ray photoelectron spectroscopy [33]. The HSE03 DOS extends to lower energies by 1 eV with respect to the PBE DOS [6] which results in a worse agreement with experiments in the position of the maximum below −10 eV.

(cf figure 14). The strongly localized HOMO state is instead localized on a cluster of square rings reminiscent of the cubic phase (cf figure 14). Due to the small size of our simulation cell we are clearly unable to address issues on the mobility edges from the analysis of KS localization.

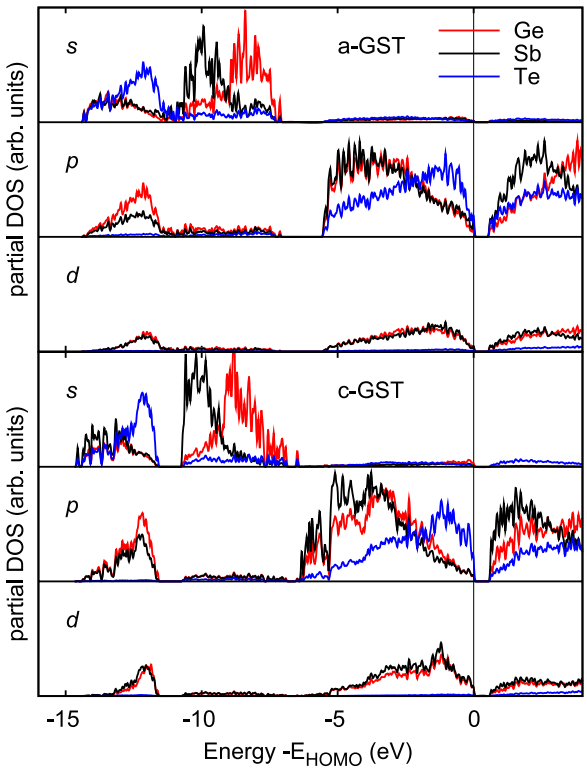

Figure 11. Electronic density of states of the stoichiometric a-GST and c-GST models projected on atomic s, p, d pseudowavefunctions.

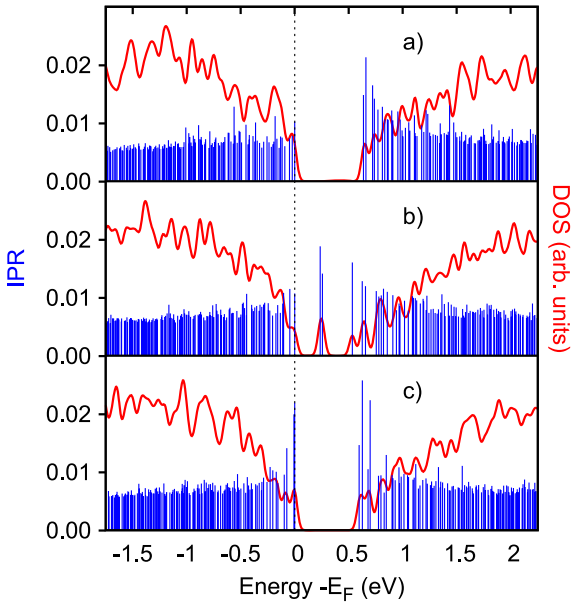

Figure 12. Electronic density of states (solid red line) and the corresponding values of the inverse participation ratio (IPR) (blue spikes, left scale, see text) close to the bandgap of stoichiometric GST in the (a) crystalline phase and in the amorphous models (b) fast-quenched [4] and (c) slow-quenched. Vertical dashed lines denote the HOMO level. The Kohn–Sham energies are broadened with Gaussian functions 27 meV wide.

In contrast to previous suggestions in the literature, we have not found long chains of Te, but Te dimers and trimers

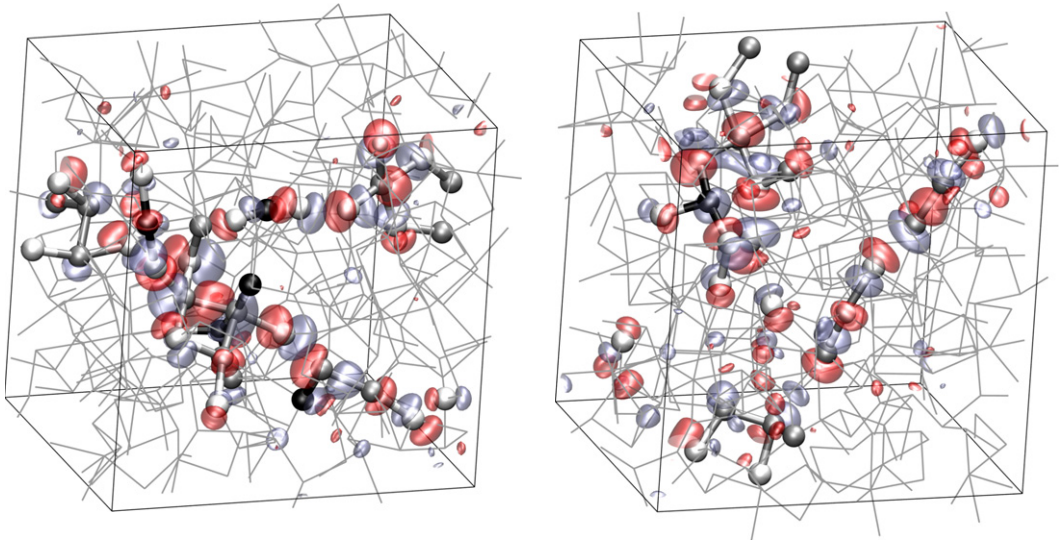

Figure 13. Snapshots of KS states in the bandgap of fast-quenched a-GST (cf figure 12): the LUMO state on the right (0.24 eV above the top of the valence band) and the LUMO + 1 state on the left (0.26 eV). Semitransparent red and blue surfaces render an isovalue of +0.012 au and −0.012 au, respectively. The whole bonding network is displayed with thin lines. The KS states are mostly localized on the atoms highlighted. Ge, Sb and Te atoms are depicted by black, grey and white spheres, respectively.

(see additional materials in our previous work [4]). The absence of long chains of Te atoms is probably also at the origin of the absence in our model of valence alternation pairs (VAPs) [13] which were suggested to be present in GST [2]. To identify the possible presence of charged defects, we computed the Bader ionic charges from the total electronic charge density by using the scheme of [43]. The calculated Bader ionic charges of the cubic rocksalt crystal and of a-GST are compared in figure 15. In a-GST, the distribution of ionic charges tails toward zero due to the presence of homopolar bonds. No highly charged defects such as VAPs are found. The Bader charges of the off-stoichiometric models (crystalline and amorphous) are similar to those of stoichiometric GST. We should also mention that in our a-GST model the precursors of VAPs in the form of one-coordinated Te or two-coordinated Sb are absent as well. We also generated a 216-atom model of a-GeTe by quenching from the melt (1000 K) in a spin-unrestricted simulation lasting 50 ps which might allow for the appearance of radical species as possible VAP precursors. The resulting amorphous model does not present, however, radical species nor VAP precursors in agreement with the lack of signals in EPR measurements on a-GeTe and a-GST films [44].

The absence of VAP species might still be due to the small size of our simulation cell whenever the expected density of VAPs would be lower than 1/270 atoms. However, we have also to consider that the fast-quenching protocol used here usually largely overestimates the concentration of the most prominent defects.

Vibrational properties. We computed the phonon frequencies of our cubic crystalline models and of a-GST models (slow and fast quenched) at stoichiometric composition by diagonalizing the dynamical matrix obtained in turn from the variation of atomic forces due to finite atomic displacements 0.0053 Å large. Only phonons with the periodicity of our supercell (Γ-point phonons) have been considered. The phonon density of states of crystalline and amorphous (slow-quenched) GST are compared in figure 16. Phonon DOS projected of the different species (Te, Sb and Ge) are also shown for a-GST and c-GST. Similar results for a-GST and c-GST have been found by Akola and Jones [6]. In an amorphous material, phonons display localization properties which depend on frequency. To address this issue, we have computed the inverse participation ratio (IPR) of the jth vibrational mode (figure 16) defined as

$$\mathrm{IPR} = \frac{\sum_\kappa \left| \frac{\mathbf{e}(j,\kappa)}{\sqrt{M_\kappa}} \right|^4}{\left(\sum_\kappa \frac{|\mathbf{e}(j,\kappa)|^2}{M_\kappa} \right)^2} \qquad (1)$$

where $\mathbf{e}(j,\kappa)$ are phonon eigenvectors and the sum over κ runs over the N atoms in the unit cell with masses M_κ. According to this definition, the value of IPR varies from $1/N$ for a completely delocalized phonon to 1 for a mode completely localized on a single atom. The values of IPR for a-GST and c-GST are reported in figure 17.

The phonon DOS of a-GST is different from that of c-GST in many respects. In a-GST the DOS displays two broad structures at 50 and 150 cm^{-1}, with the former sizably higher than the latter, while in the DOS of crystalline GST we can still recognize two structures at 50 and 150 cm^{-1} but along with a third, broader and more intense peak at 90 cm^{-1}. In c-GST, the first peak at 50 cm^{-1} is mostly due to the motion of undercoordinated Te atoms (nearest neighbors to vacancies) as emerges from figure 18 which shows the DOS projected on Te atoms with different coordination numbers. In a-GST, the lower the coordination the higher is the contribution of Te to the first peak at 50 cm^{-1} (cf figure 18). Moreover, the DOS projected on Ge and Sb with low coordinations show a more pronounced minimum at ∼100 cm^{-1} and sharper peaks at lower (50 cm^{-1}) and higher (150 cm^{-1}) frequencies with

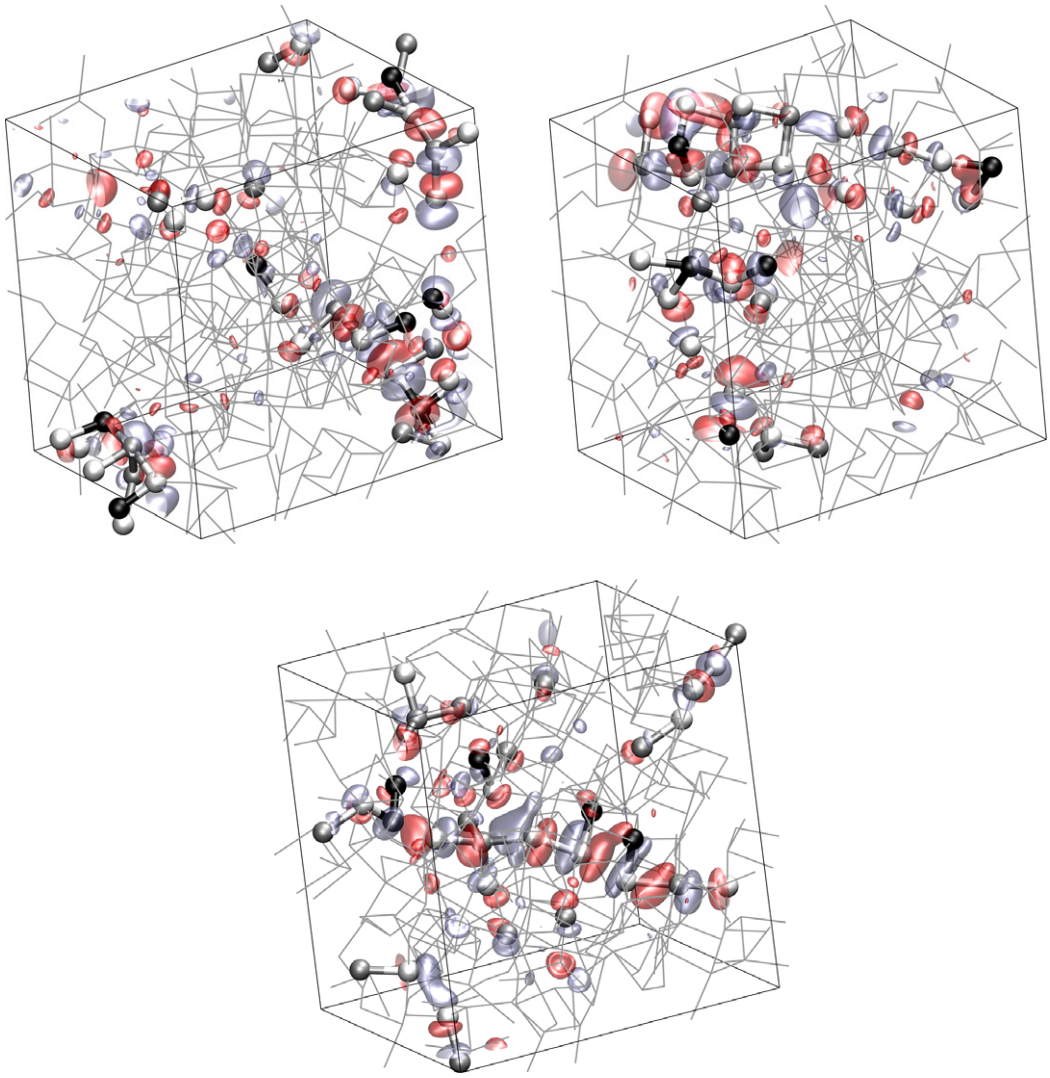

Figure 14. Snapshots of KS states in the bandgap of slow-quenched a-GST (cf figure 12): the HOMO state (upper panel) and the two mostly localized states near the edge of the conduction band in the central (state at 0.63 eV) and bottom (at 0.7 eV) panels. Semitransparent red and blue surfaces render an isovalue of +0.012 au and −0.012 au, respectively. The whole bonding network is displayed with thin lines. The KS states are mostly localized on the atoms highlighted. The color code is the same as in figure 13.

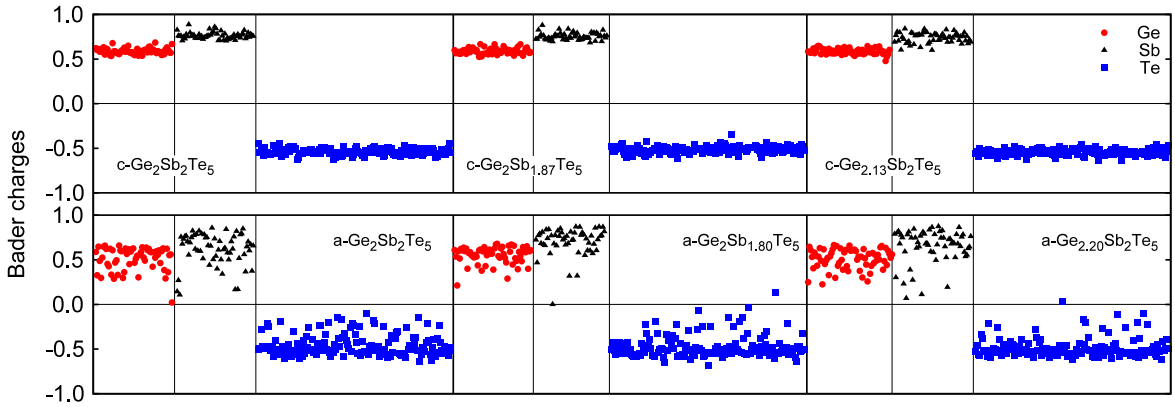

Figure 15. Bader ionic charges (atomic units) of models of cubic (upper panels) and amorphous GST (lower panels) at stoichiometric (left panels) and off-stoichiometric (central and right panels) compositions. Each point corresponds to an individual atom in the 270-atom supercell.

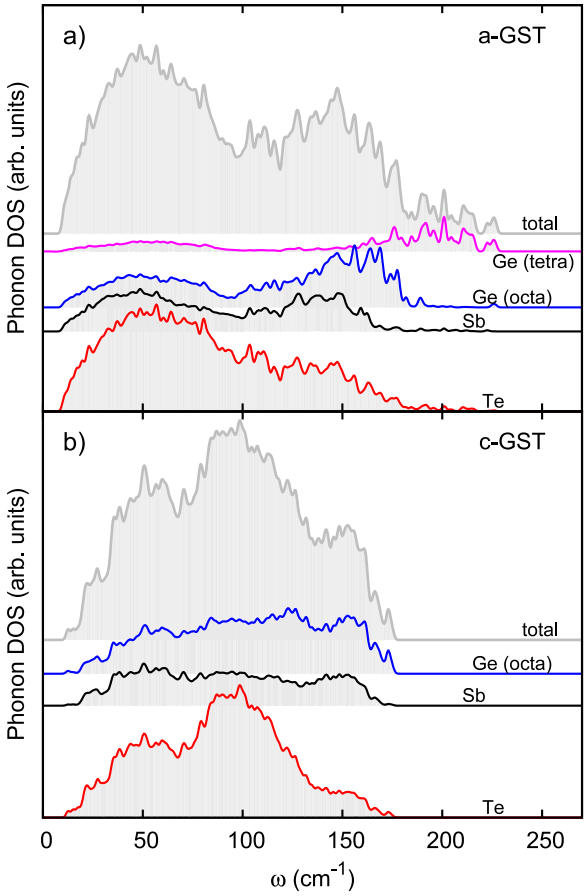

Figure 16. Phonon density of states (DOS) of (a) a-GST and (b) c-GST. Projection of the phonon DOS on different species (Te, Sb and Ge in tetrahedral (tetra) and defective octahedral (octa) sites) are also reported. The contribution to the DOS of the jth mode with eigenvector $\mathbf{e}(j,\kappa)$ is multiplied by $\sum_\kappa \frac{|\mathbf{e}(j,\kappa)|^2}{M_\kappa}$, where the sum over κ is restricted to atoms of a given species with mass M_κ.

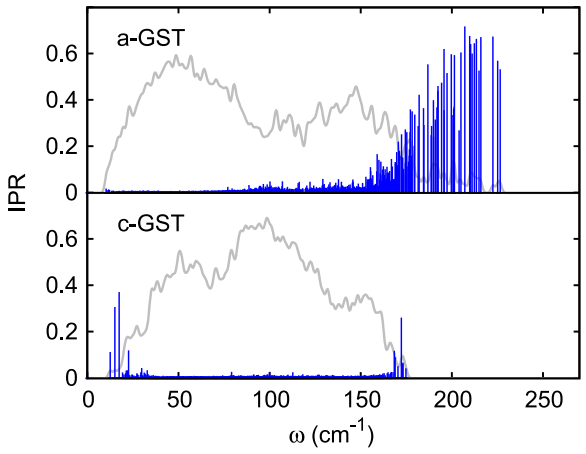

Figure 17. Inverse participation ratio (IPR) for phonons in a-GST and c-GST (blue spikes, left scale, see text) superimposed on the density of states of figure 16.

respect to projections on Ge and Sb with higher coordinations (cf figure 19).

In a-GST, the modes above 175 cm^{-1}, i.e. above the upper edge of the DOS in the crystalline phase, are strongly localized

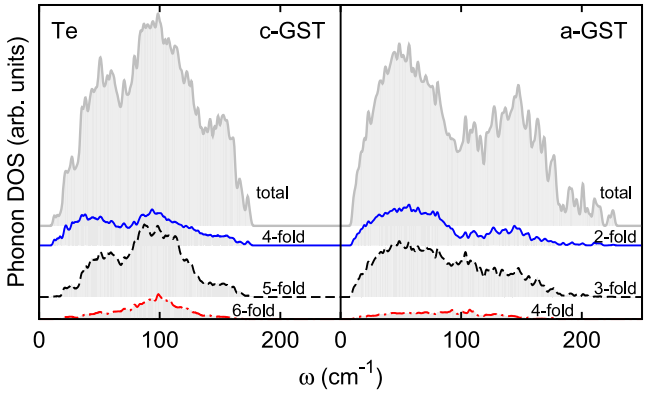

Figure 18. Phonon density of states of c-GST and a-GST projected on Te atoms with different coordination.

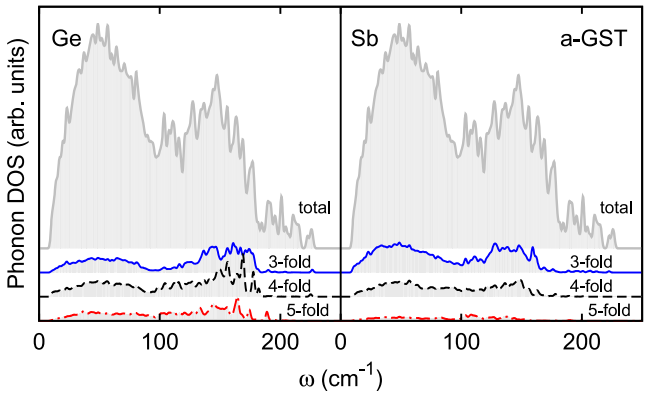

Figure 19. Phonon density of states of a-GST projected on Ge (octahedral) or Sb atoms with different coordination.

mostly on Ge atoms in tetrahedral sites (cf figure 16). The projection of the phonon DOS on Ge atoms bonded only to Te or also to Ge/Sb, reported in figure 20, reveals that the localized states above 175 cm^{-1} are indeed associated with the tetrahedral environment and not with the presence of 'wrong bonds'. Indeed, tetrahedral Ge atoms bonded with Te only give rise to localized modes above 175 cm^{-1}.

From the experimental side, information on the vibrational spectra of cubic and amorphous GST are available from Raman scattering [34, 45] and coherent phonon spectroscopy [46]. The measured phonon frequencies fall within the range of the DOS in figure 16 for both a-GST and c-GST. However, both experimental techniques reveal only particular phonons which are difficult to be predicted on the basis of displacement pattern only. A meaningful comparison between theory and experiments would require the calculation of Raman tensors which is computationally very demanding and is left for future work. We computed the Debye–Waller factor for each species defined by [47]

$$B_\kappa = \frac{8\pi^2}{3}\langle \mathbf{u}_\kappa^2 \rangle$$

where κ runs over the three species and $\langle \mathbf{u}_\kappa^2 \rangle$ is the mean average square displacement of atoms of species κ computed

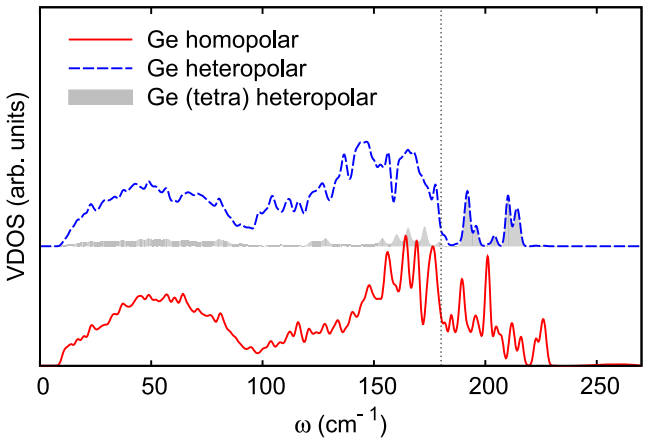

Figure 20. Phonon density of states of a-GST projected on Ge atoms bonded only to Te (heteropolar) or bonded also to Ge/Sb (homopolar bonds). In the former case further projection on Ge in a tetrahedral site is shown as a shaded area.

from harmonic phonons as

$$\langle \mathbf{u}_\kappa^2 \rangle = \frac{1}{N_\kappa} \sum_{j,m} \frac{\hbar}{\omega_j} \frac{|\mathbf{e}(j,m)|^2}{M_\kappa} \left[n_{\mathrm{B}}\left(\frac{\hbar\omega_j}{k_{\mathrm{B}}T}\right) + \frac{1}{2} \right], \quad (2)$$

where M_κ is the mass of the κth species, m runs over N_κ atoms of species κ, while ω_j and $\mathbf{e}(j,m)$ are the frequency and eigenvector of the jth harmonic phonon. The temperature dependence is introduced by the Bose factor $n_{\mathrm{B}}(\frac{\hbar\omega_j}{k_{\mathrm{B}}T})$.

The resulting Debye–Waller factors as a function of temperature are reported in figure 21 for a-GST and c-GST. For the crystal, the static mean square displacement with respect to the ideal rocksalt geometry is added to the vibrational contribution to B_κ in order to compare with experimental values inferred from the Rietveld analysis of XRD data. For crystalline GST at 300 K, the calculated Debye–Waller factor averaged over the different species ($B_{\mathrm{ave}} = \frac{2}{9}(B_{\mathrm{Ge}} + B_{\mathrm{Sb}}) + \frac{5}{9}B_{\mathrm{Te}} = 2.47$ Å^2) is in very good agreement with XRD data ($B_{\mathrm{ave}} = 2.51$ Å^2 in [32] or $B_{\mathrm{ave}} = 2.44$ Å^2 in [22]). However, the difference among the partial B_κ is much smaller in our model than in experiments, namely $B_{\mathrm{Ge}} = 3.15$ Å^2, $B_{\mathrm{Sb}} = 2.62$ Å^2 and $B_{\mathrm{Te}} = 2.14$ Å^2 (300 K) in our model while $B_{\mathrm{Ge}} = 4.2(3)$ Å^2, $B_{\mathrm{Sb}} = 3.2(3)$ Å^2 and $B_{\mathrm{Te}} = 1.57(3)$ Å^2 from the Rietveld analysis of [32]. Since the dependence of the experimental Debye–Waller factor on temperature ($\mathrm{d}B/\mathrm{d}T$) is very well reproduced by our results, the disagreement fully comes from the static mean square displacement with respect to the ideal rocksalt geometry. Actually, $\mathrm{d}B/\mathrm{d}T = 0.004\,35$ (Ge/Sb) and $0.003\,85$(Te) Å^2 K^{-1} in our simulations are to be compared to the experimental values of $\mathrm{d}B/\mathrm{d}T = 0.004\,30$ (Ge/Sb) and $0.003\,80$ (Te) Å^2 K^{-1} from [48]. The static contributions to B_κ can be read from figure 21 from the intersection of the curves with the ordinate axis (1.67 Å^2, 1.44 Å^2 and 0.96 Å^2 for Ge, Sb and Te, respectively). In other words, Ge/Sb atoms are less displaced from the rocksalt positions while Te atoms are more displaced with respect to what is inferred from the Rietveld analysis in [22]. The distribution of the displacement lengths of Ge, Sb and Te with respect to the ideal rocksalt geometry in cubic GST is given in figure 22.

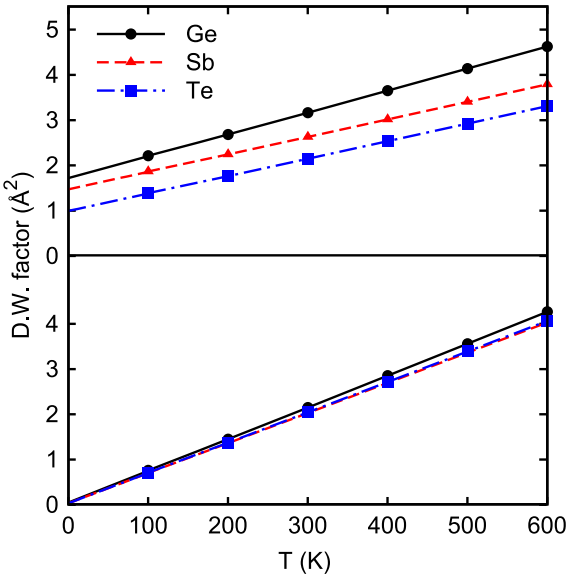

Figure 21. Debye–Waller B factor (see text) for Te, Ge and Sb atoms for crystalline (upper panel) and amorphous (lower panel) stoichiometric GST as a function of temperature. For crystalline GST, the mean square displacement is considered with respect to the ideal rocksalt geometry to compare with experimental XRD data [22]. The static contributions to B_κ can be read from the intersection of the curves with the ordinate axis (see text).

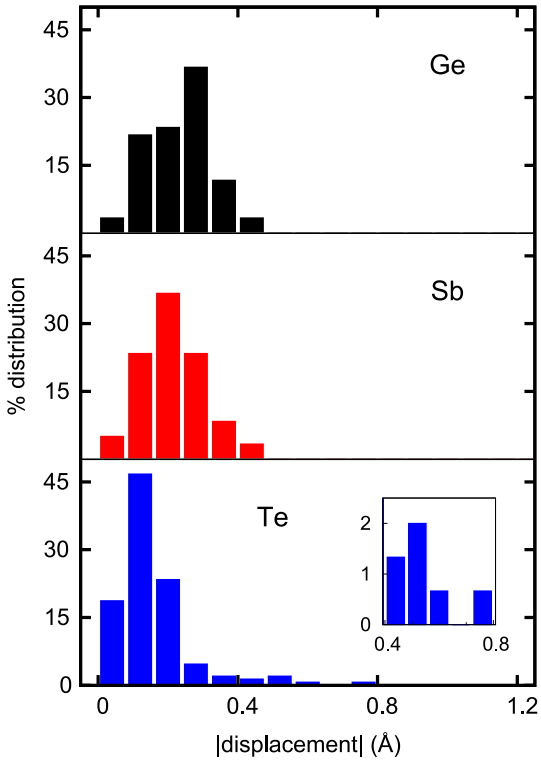

Figure 22. Distribution of the displacement lengths of Ge, Sb and Te with respect to the ideal rocksalt geometry in cubic GST.

In agreement with previous *ab initio* calculations on GST [49] and $GeSb_2Te_4$ [30], but in contrast to the simple electrostatic argument of [34], Te atoms move mostly toward the nearest-neighbor vacancy. In contrast Ge and Sb mostly move away from the vacancy once only a single vacancy is present in the next-nearest-neighbor coordination shell. The displacement is more complex and environment-dependent when Ge and Sb are next-nearest neighbors to more than one vacancy.

Concerning a-GST, the Debye–Waller factors do not show a strong dependence on the chemical species (Sb/Ge or Te) and are, on average, close to the crystalline values once only the thermal contribution is considered. Although the independence of the Debye–Waller factor on the chemical species shown experimentally is reproduced by the theory [48], our calculated Debye–Waller factors for a-GST are more than three times larger than the values inferred experimentally from EXAFS data [48]. The reasons behind this disagreement remain to be investigated further. Overall our calculations indicate that the thermal mean square displacements in the crystalline and amorphous phases are similar, in contrast with the EXAFS data [48]. Similar results for the Debye–Waller factors are obtained with the LDA functional (at the theoretical equilibrium volumes) with deviations with respect to PBE results of about 5%.

4. Conclusions

Based on DFT calculations we have investigated the change in the electronic density of states of crystalline and amorphous GST induced by stoichiometric defects. While in the crystalline phase Sb/Ge deficiency (excess) induces a shift of the Fermi level into the valence (conduction) band, in the amorphous phase the HOMO level is pinned at the top of the valence band (and the Fermi level at the center of the bandgap) also in the presence of Ge/Sb excess or deficiency. Our results support the conjecture that the p-type degenerate character of cubic GST was induced by defects in stoichiometry, most probably Sb vacancies. The same defects, however, are unable to turn the amorphous phase into a degenerate semiconductor, consistently with the large change in resistivity across the phase change measured experimentally. The electronic properties of a-GST seem thus rather robust with respect to small changes in composition. This result is of great relevance for applications in PCM whose realization could thus tolerate small deviations in the stoichiometry of GST. No VAP states are found in our (small) models of a-GST. The simulations also revealed that the use of a hybrid exchange and correlation functional (HSE03 or PBE0) in the geometry optimization of an a-GST model generated at the PBE level induces a 2% shortening of the Ge–Te bond lengths which, however, are still 5% longer compared to EXAFS data [34, 35, 37, 38]. For stoichiometric GST we have also analyzed the vibrational spectrum which revealed the presence of high frequency modes, outside the phonon spectral range of the cubic phase, which are due to vibrations of Ge in tetrahedral sites in agreement with the results of [6]. The mean square displacement of Ge/Sb is larger than that of Te in the cubic phase while all the species have similar Debye–Waller factors in the amorphous phase. Once averaged over the different species, the Debye–Waller factors (due to thermal motion only) of the crystalline and amorphous phases turn out to be very similar.

Acknowledgments

We gratefully acknowledge the computational resources, technical expertise and assistance provided by the Barcelona Supercomputing Center—Centro Nacional de Supercomputación, by the DEISA Consortium under project PHASEMAT, by CSCS (Manno, CH) and by INFM-CNR-CNISM parallel computing initiative at CINECA. Discussions with R Bez, A Modelli, A Pirovano and E Varesi are gratefully acknowledged. SC acknowledges support through SNSF (no. 200021-119882).

References

[1] Lacaita A L and Wouters D J 2008 *Phys. Status Solidi* a **205** 2281
[2] Pirovano A, Lacaita A L, Benvenuti A, Pellizzer F and Bez R 2004 *IEEE Trans. Electron Devices* **51** 452
[3] Wuttig M and Yamada N 2007 *Nat. Mater.* **6** 824
[4] Caravati S, Bernasconi M, Kühne T D, Krack M and Parrinello M 2007 *Appl. Phys. Lett.* **91** 171906
[5] Akola J and Jones R O 2007 *Phys. Rev.* B **76** 235201
[6] Akola J and Jones R O 2008 *J. Phys.: Condens. Matter* **20** 465103
[7] Hegedüs J and Elliott S R 2008 *Nat. Mater.* **7** 399
[8] Lencer D, Salinga M, Grabowski B, Hickel T, Neugebauer J and Wuttig M 2008 *Nat. Mater.* **7** 972
[9] Wełnic W, Botti S, Reining L and Wuttig M 2007 *Phys. Rev. Lett.* **98** 236403
[10] Robertson J, Xiong K and Peacock P W 2007 *Thin Solid Films* **515** 7538
[11] Baily S A, Emin D and Li H 2006 *Solid State Commun.* **139** 161
[12] Redaelli A, Pirovano A, Benvenuti A and Lacaita A L 2008 *J. Appl. Phys.* **103** 111101
[13] Kastner M, Adler D and Fritzshe H 1976 *Phys. Rev. Lett.* **37** 1504
[14] Ielmini D and Zhang Y 2007 *J. Appl. Phys.* **102** 054517
[15] Lee B-S, Abelson J R, Bishop S G, Kang D-H, Cheong B-K and Kim K-B 2005 *J. Appl. Phys.* **97** 093509
[16] Heyd J, Scuseria G E and Ernzerhof M 2003 *J. Chem. Phys.* **118** 8207
[17] Kühne T D, Krack M, Mohamed F R and Parrinello M 2007 *Phys. Rev. Lett.* **98** 066401
[18] Krack M and Parrinello M 2004 *High Performance Computing in Chemistry* (*NIC* vol 25) ed J Grotendorst, pp 29–51 http://cp2k.berlios.de.
[19] VandeVondele J, Krack M, Mohamed F, Parrinello M, Chassaing T and Hutter J 2005 *Comput. Phys. Commun.* **167** 103
[20] Perdew J P, Burke K and Ernzerhof M 1996 *Phys. Rev. Lett.* **77** 3865
[21] Goedecker S, Teter M and Hutter J 1996 *Phys. Rev.* B **54** 1703
Krack M 2005 *Theor. Chem. Acc.* **114** 145
[22] Matsunaga T, Yamada N and Kubota Y 2004 *Acta Crystallogr.* B **60** 685
[23] Nonaka T, Ohbayashi G, Toriumi Y, Mori Y and Hashimoto H 2000 *Thin Solid Films* **370** 258
[24] Yamada N and Matsunaga T 2000 *J. Appl. Phys.* **88** 7020

[25] Njoroge W K, Wöltgens H W and Wuttig M 2002 *J. Vac. Sci. Technol.* A **20** 230
[26] Ernzerhof M and Scuseria G E 1999 *J. Chem. Phys.* **110** 5029
Adamo C and Barone V 1999 *J. Chem. Phys.* **110** 6158
[27] Krukau A V, Vydrov O A, Izmaylov A F and Scuseria G E 2006 *J. Chem. Phys.* **125** 224106
[28] Staroverov V N, Scuseria G E, Tao J and Perdew J P 2003 *J. Chem. Phys.* **119** 12129
Staroverov V N, Scuseria G E, Tao J and Perdew J P 2003 *J. Chem. Phys.* **121** 11507 (erratum)
[29] Edwards A H, Pineda A C, Schultz P A, Martin M G, Thompson A P, Hjalmarson H P and Umrigar C J 2006 *Phys. Rev.* B **73** 045210
[30] Wuttig M, Lüsebrink D, Wamwangi D, Wełnic W, Gilleßen M and Dronskowski R 2007 *Nat. Mater.* **6** 122
[31] Keen D A 2001 *J. Appl. Crystallogr.* **34** 172
[32] Shamoto S I, Kodama K, Iikubo S, Taguchi T, Yamada N and Proffen T 2006 *Japan. J. Appl. Phys.* **45** 8789
[33] Kim J-J, Kobayashi K, Ikenaga E, Kobata M, Ueda S, Matsunaga T, Kifune K, Kojima R and Yamada N 2007 *Phys. Rev.* B **76** 115124
[34] Kolobov A V, Fons P, Frenkel A I, Ankudinov A L, Tominaga J and Uruga T 2004 *Nat. Mater.* **3** 703
[35] Jóvári P, Kaban I, Steiner J, Beuneu B, Schöps A and Webb M A 2008 *Phys. Rev.* B **77** 035202
[36] Giacomazzi L, Umari P and Pasquarello A 2006 *Phys. Rev.* B **74** 155208
[37] Baker D A, Paesler M A, Lucovsky G, Agarwal S C and Taylor P C 2006 *Phys. Rev. Lett.* **96** 255501
[38] Jóvári P, Kaban I, Steiner J, Beuneu B, Schöps A and Webb M A 2007 *J. Phys.: Condens. Matter* **19** 335212
[39] Kohara S *et al* 2006 *Appl. Phys. Lett.* **89** 201910
[40] Steimer C, Coulet V, Welnic W, Dieker H, Detemple R, Bichara C, Beuneu B, Gaspard J-P and Wuttig M 2008 *Adv. Mater.* **20** 4535
[41] Kolobov A V *et al* 2006 *Phys. Rev. Lett.* **97** 035701
[42] Caravati S, Bernasconi M, Kühne T D, Krack M and Parrinello M 2009 *Phys. Rev. Lett.* **102** 205502
[43] Henkelman G, Arnaldsson A and Jonsson H 2006 *Comput. Mater. Sci.* **36** 354
[44] Olson J K, Li H, Ju T, Viner J M and Taylor P C 2006 *J. Appl. Phys.* **99** 103508
[45] De Bastiani R, Piro A M, Grimaldi M G, Rimini E, Baratta G A and Strazzulla G 2008 *Appl. Phys. Lett.* **92** 241925
[46] Först M, Dekorsy T, Trappe C, Laurenzis M, Kurz H and Béchevet B 2000 *Appl. Phys. Lett.* **77** 1964
[47] Peng L-M, Dudarev S L and Whelan M J 2004 *High Energy Electron Diffraction and Microscopy* (Oxford: Oxford University Press)
[48] Matsunaga T, Kojima R, Yamada N, Tanida H, Uruga T and Kohara S 2008 *Proc. EPCOS 2008 Conf.* available online at http://www.epcos.org/library/Library2008.htm
[49] Lang C, Song S A, Manh D N and Cockayne D J H 2007 *Phys. Rev.* B **76** 054101